Computer Physics Communications 242 (2019) 49–59

Contents lists available at ScienceDirect

Computer Physics Communications

journal homepage: www.elsevier.com/locate/cpc

A fast and accurate numerical implementation of the envelope model for laser–plasma dynamics

Davide Terzani [a,*,1,2,3], Pasquale Londrillo [b,4,5]

[a] INO-CNR Sezione di Pisa, Via Giuseppe Moruzzi 1, 56124 Pisa, Italy
[b] INAF, Osservatorio Astronomico di Bologna, Via Gobetti 93/3, Bologna, Italy

ARTICLE INFO

Article history:
Received 3 August 2018
Received in revised form 1 March 2019
Accepted 12 April 2019
Available online 18 April 2019

Keywords:
Laser–plasma acceleration
Particle-in-cell
Reduced computational model
Cold fluid plasma numerical integration

ABSTRACT

In laser-driven, plasma wakefield acceleration regimes (LWFA), when relevant scale lengths of the laser envelope and of the driven plasma waves are well separated from the wavelength and frequency of the laser fast oscillating component, a reduced physical model (usually referred to as the envelope model), has been introduced, allowing to formulate the laser–plasma equations in terms of laser cycle-averaged dynamical variables. As a main consequence, physical regimes where this reduced model applies, can be investigated with significant savings of computational resources still assuring comparable accuracy, with respect to standard Particle-In-Cell (PIC) models where all relevant space–time scales have to be resolved.

Here we propose a computational framework characterized by two previously unexplored numerical implementations of the envelope model. The first one is based on explicit second order leapfrog integration of the exact wave equation for laser pulse propagation in a laboratory coordinate system in 3D cartesian geometry, replacing the usually quoted representation in an Eulerian frame moving at the speed of light. Since the laser and driven wakefield wave equations in a laboratory frame are advection dominated, we introduce a proper modification of finite differences approximating longitudinal space derivatives, to minimize dispersive numerical errors coming from the discretized advection operators. The proposed implementation, avoiding semi-implicit procedures otherwise required when dealing with a comoving frame, assures significant saving in computational time and ease of implementation for parallel platforms. The associated equation of motion for plasma particles has been integrated, as in standard PIC codes, using the Boris pusher, properly extended to take into account the specific form of the Lorentz force in the envelope model.

As a second contribution, a novel numerical implementation of the plasma dynamics equations in the cold-fluid approximation, is presented. The scheme is based on the second-order one-step Adams–Bashforth time integrator coupled to upwind non-oscillatory WENO reconstruction for discretized space derivatives. The proposed integration scheme for the Eulerian fluid equations is equivalent to a leapfrog scheme with an added higher order dissipative truncation errors. It can be used either as a much faster, yet of comparable accuracy, alternative to the PIC representation of plasma particle motion, or even in a hybrid fluid–particle combination when kinetic effects and particle injection and acceleration in a wakefield have to be investigated.

1. Introduction

The general formal setting describing laser–plasma interaction in LWFA, usually referred to as Vlasov–Maxwell system, is represented by the relativistic equation of motion of N_p discrete plasma particles (electron or positrons) with $(\mathbf{p}_\alpha(t),\ \mathbf{x}_\alpha(t))$ $\alpha = 1, 2, \ldots, N_p$ phase space coordinates and (q, m) charge and mass, respectively, coupled to the Maxwell equation evolving the self-consistent $(\mathbf{E}, \mathbf{B})$ fields under the mean-field approximation. The Klimontovitch formalism based on delta functions $\delta[\mathbf{x}-\mathbf{x}_\alpha(t)]$, or, as more appropriate when dealing with numerical PIC implementation, using delta-like smoothing shape functions $\hat{S}[\mathbf{x}-\mathbf{x}_\alpha(t)]$, is then applied to connect discrete point particles to continuous fields. In this formalism, particle density $n(\mathbf{x}, t)$ and current density $\mathbf{J}(\mathbf{x}, t)$ are defined, respectively, by

$$n(\mathbf{x}, t) = \sum_\alpha \hat{S}[\mathbf{x} - \mathbf{x}_\alpha(t)], \quad \mathbf{J}(\mathbf{x}, t) = q \sum_\alpha \mathbf{v}_\alpha(t)\hat{S}[\mathbf{x} - \mathbf{x}_\alpha(t)], \quad (1)$$

* Corresponding author.
E-mail address: davide.terzani@ino.it (D. Terzani).
1 INO-CNR Sezione di Pisa, Pisa, Italy.
2 INFN Sezione di Napoli, Napoli, Italy.
3 Dipartimento di Fisica, Università di Napoli "Federico II", Italy.
4 INAF Sezione di Bologna, Bologna, Italy.
5 Dipartimento di Fisica e Astronomia, Università di Bologna, Italy.

https://doi.org/10.1016/j.cpc.2019.04.007
0010-4655/

and, by converse, the field assignment to each particle position is expressed by:

$$\mathbf{E}(\mathbf{x}_\alpha, t) = \int d\mathbf{x}\hat{S}[\mathbf{x} - \mathbf{x}_\alpha(t)]\mathbf{E}(\mathbf{x}, t),$$
$$\mathbf{B}(\mathbf{x}_\alpha, t) = \int d\mathbf{x}\hat{S}[\mathbf{x} - \mathbf{x}_\alpha(t)]\mathbf{B}(\mathbf{x}, t). \tag{2}$$

The particle equations of motion in dimensionless variables are given by:

$$\frac{d\mathbf{p}_\alpha}{dt} = \frac{q\omega_p}{m}\left[\mathbf{E}(\mathbf{x}_\alpha, t) + \frac{\mathbf{v}_\alpha}{c} \times \mathbf{B}(\mathbf{x}_\alpha, t)\right],$$
$$\frac{d\mathbf{x}_\alpha}{dt} = \mathbf{v}_\alpha = \frac{c\mathbf{p}_\alpha}{\gamma_\alpha}, \quad \gamma_\alpha = \sqrt{1 + |\mathbf{p}_\alpha|^2}, \tag{3}$$

while the evolutionary pair of field Maxwell equation is given by:

$$\partial_t \mathbf{B} = -c\nabla \times \mathbf{E}, \quad \partial_t \mathbf{E} = c\nabla \times \mathbf{B} - \omega_p \mathbf{J}. \tag{4}$$

Here all variables are expressed in dimensionless form, so that charge and mass are normalized respectively to electron charge and mass e, m_e (*e.g.* the coupling constant in the equations of motion for an electron is $q/m = -1$), particles momenta are normalized to mc, plasma density is normalized to the background electron density n_0, current is normalized to ecn_0, electric and magnetic fields are normalized to $E_0 = B_0 = A_0 k_p$, where $A_0 = m_e c^2/e$ is the normalization unit for the associated $\mathbf{A}(\mathbf{x}, t)$ vector potential and $\omega_p = ck_p = \sqrt{4\pi e^2 n_0/m_e}$ is the electron plasma frequency.

To introduce the envelope model for the Vlasov–Maxwell equation, one considers that in typical Laser Plasma Accelerator (LPA) configurations, a polarized laser field propagating along the z coordinate, when represented in terms of the normalized vector potential $\mathbf{a}(\mathbf{x}, t) = \mathbf{A}(\mathbf{x}, t)/A_0$, under the Coulomb gauge $\nabla \cdot \mathbf{a} = 0$, can be modeled by an envelope shape function modulated by a fast oscillating monochromatic component

$$\mathbf{a}(\mathbf{x}, t) = \mathcal{R}e\left[\hat{\mathbf{a}}(\mathbf{x}, t)e^{ik_0(z-ct)}\right], \tag{5}$$

where $k_0 = 2\pi/\lambda_0$, $\omega_0 = ck_0$ is the carrier laser space–time frequency. In this representation, the complex envelope function $\hat{\mathbf{a}}(\mathbf{x}, t)$ depends on slower space–time scales, that is the spectral modes of $\hat{\mathbf{a}}(\mathbf{k}, \omega)$ have sizes $\omega/\omega_0 \sim k/k_0 = \mathcal{O}(\varepsilon)$ where ε is a small number. In numerical investigation of LPA regimes, the $\hat{\mathbf{a}}(\mathbf{x}, t)$ field is initialized in vacuum in the form $\hat{\mathbf{a}}(\mathbf{x}, t) = f(z - ct)\mathbf{g}(\mathbf{x})$ where $\mathbf{g}$ has a Gaussian shape along the transverse $r = \sqrt{x^2 + y^2}$ coordinate, characterized by a waist $w_0 \gg \lambda_0$ at the $z = z_f$ focal point and $f(z - ct)$ is a Gaussian-like shape function with scale $L_z \gg \lambda_0$ along the comoving $\xi = z - ct$ longitudinal coordinate. In this configuration, the small parameter measuring scale separation is defined by $\varepsilon = 1/(k_0 w_0) \simeq 1/(k_0 L_z) \ll 1$. To the lowest order approximation, a Gaussian field has a $\mathcal{O}(1)$ field component $\mathbf{a}_\perp = (a_x, a_y)$, where $|a_y| = |a_x|$ for circular polarization, or $a_y = \mathcal{O}(\varepsilon^2)$ for linear polarization along the x coordinate, whereas the longitudinal component has size $a_z = \mathcal{O}(\varepsilon)$. On the assumption that scale separation set by initial conditions is preserved in time during laser propagation, that is scale lengths l_p of the plasma density variations satisfy $1/k_0 l_p = \mathcal{O}(\varepsilon)$, a two-scale perturbative analysis can then be applied [1–3] to reformulate the Vlasov–Maxwell system in terms of laser cycle-averaged dynamical variables depending only on slow space–time coordinates.

By referring to the cited works for a detailed derivation of the envelope model, in Section 2 the resulting set of plasma and field equations of motion, are first shortly reported. Section 3 is devoted to the field solvers, where we present and discuss the details of the implementation of numerical schemes for the laser envelope and wake fields propagation. In Section 4, the numerical integration of Lagrangian equation of motion for PIC particles, by extending the classical Boris pusher to the envelope model, is then presented and discussed, whereas Section 5 contains the presentation of a numerical integration of the plasma equations in Eulerian fluid variables. Finally, Section 6 contains validations and benchmarks of our schemes.

2. The envelope model equations

The envelope model has been derived using multi-scale perturbative procedures on the equation of motion either in Lagrangian form equation (3), (see [3,4] and references therein) or in Eulerian form for plasma momenta $\mathbf{p}(\mathbf{x}, t)$ derived from the Vlasov equation in the cold-fluid approximation, see [1]. We shortly report here the main results derived in the Eulerian approach, where the formulation appears more convincing and self-contained. These results can then be applied for a system of discrete Lagrangian particles by projection of fluid variables onto the particle phase space coordinates.

In the Eulerian approach, fluid momentum $\mathbf{p}(\mathbf{x}, t)$ (and all related dynamical variables) is split into two components: $\mathbf{p} = \bar{\mathbf{p}} + \delta\mathbf{p}$, where the cycle-averaged part $\bar{\mathbf{p}}(\mathbf{x}_1, t_1)$ depends only on the slow space–time coordinates $t_1 = \varepsilon\omega_0 t$, $\mathbf{x}_1 = \varepsilon k_0 \mathbf{x}$ and the residual part $\delta\mathbf{p}(t_1, \mathbf{x}_1; t_0, z_0)$ depends both on the slow and fast $t_0 = \omega_0 t$, $z_0 = k_0 z$ coordinates. Correspondingly, the plasma current density induced by the plasma fluid motion is split into components $\mathbf{J} = \bar{\mathbf{J}} + \delta\mathbf{J}$. The averaged component acts as a source term of the Maxwell equation expressed by Eq. (4), now evolving the driven wakefield ($\mathbf{E}$, $\mathbf{B}$) on the slow space–time scales, whereas the oscillatory part $\delta\mathbf{J}$ acts as a source term of a separate Maxwell equation evolving the laser field, represented by the dominant vector potential components

$$\left[\partial_{t,t} - c^2\nabla^2\right]\mathbf{a}_\perp = \omega_p^2 \delta\mathbf{J}_\perp. \tag{6}$$

In the two-scale perturbative analysis [1] of the momentum equation, the leading order solution for the oscillatory momentum component is given by $\delta\mathbf{p}_\perp = -q\mathbf{a}_\perp/m$, whereas the longitudinal δp_z component has size $\mathcal{O}(\varepsilon)$ smaller. As a first consequence, the particle γ function is approximated by $\gamma = \bar{\gamma} + \mathcal{O}(\varepsilon^2)$, where the cycle-averaged part is $\bar{\gamma} = \left(1 + |\bar{\mathbf{p}}|^2 + q^2|\hat{a}|^2/2m^2\right)^{1/2}$. The oscillatory and averaged current density components can now be expressed, respectively, by

$$\delta\mathbf{J}_\perp = q\bar{n}\frac{\delta\mathbf{p}_\perp}{\bar{\gamma}}, \quad \bar{\mathbf{J}} = q\bar{n}\frac{\bar{\mathbf{p}}}{\bar{\gamma}} \tag{7}$$

where $\bar{n}$ is the cycle-averaged plasma density satisfying the continuity equation

$$\partial_t \bar{n} + \nabla \cdot (n\bar{\mathbf{v}}) = 0, \quad \bar{\mathbf{v}} = \frac{c\bar{\mathbf{p}}}{\bar{\gamma}}. \tag{8}$$

By inserting the $\delta\mathbf{J}_\perp$ relation of Eq. (7) in (6), the fast oscillating phase part of the $\mathbf{a}_\perp$ field is factored out, leading to a closed equation for the envelope function $\hat{a}$ in complex form:

$$\left[\partial_{t,t} - 2i\omega_0(\partial_t + c\partial_z) - c^2\nabla^2\right]\hat{a}(\mathbf{x}, t) = -\omega_p^2 \chi(\mathbf{x}, t, |\hat{a}|)\hat{a}(\mathbf{x}, t), \tag{9}$$

where $\chi(\mathbf{x}, t, |\hat{a}|) = q^2\bar{n}/\bar{\gamma}$ and all dynamical variables depend only on slow space–time coordinates (here denoted as $(\mathbf{x}, t)$).

The second main achievement of the envelope modelization is the relation expressing the cycle-averaged laser Lorentz force acting on the plasma fluid (here specialized to linear polarization)

$$\mathbf{F}_L = -\frac{1}{2\bar{\gamma}}\nabla\Phi, \quad \Phi = \frac{q^2|\hat{a}|^2}{2m^2}. \tag{10}$$

The equation of motion for the averaged plasma momentum $\overline{\mathbf{p}}(\mathbf{x}, t)$, can now be expressed in closed form by

$$\left[\partial_t + \overline{\mathbf{v}} \cdot \nabla\right] \overline{\mathbf{p}} = \frac{q\omega_p}{m} \left[\mathbf{E}(\mathbf{x}, t) + \frac{\mathbf{p}}{\overline{\gamma}} \times \mathbf{B}(\mathbf{x}, t)\right] + \mathbf{F}_L(\mathbf{x}, t), \tag{11}$$

where the total Lorentz force is split into a contribution due to the wake fields and a contribution coming from the laser ponderomotive force $\mathbf{F}_L$.

In the Lagrangian framework, a two-scale perturbative analysis of the equation of motion for particle $[\mathbf{x}_\alpha(t),\ \mathbf{p}_\alpha(t)]$ phase-space coordinates has been formulated in [3,4], often denoted as ponderomotive guiding center (PGC) modeling, where the cycle-averaged $[\overline{\mathbf{x}}_\alpha(t_1),\ \overline{\mathbf{p}}_\alpha(t_1)]$ coordinates evolving on slow time scales describe the guiding center motion and the residual components $[\delta\mathbf{x}_\alpha,\ \delta\mathbf{p}_\alpha]$ describe the oscillatory motion around the guiding center. Using averaged momentum in the Eulerian variables of Eq. (11) and by defining the momentum of the particle guiding center by

$$\overline{\mathbf{p}}_\alpha(t) = \int d\mathbf{x} \hat{S}[\mathbf{x} - \overline{\mathbf{x}}_\alpha(t)] \overline{\mathbf{p}}(\mathbf{x}, t), \tag{12}$$

Eq. (11) can be formulated in a PGC Lagrangian framework as

$$\begin{aligned} &\frac{d\mathbf{p}_\alpha(t)}{dt} = \frac{q\omega_p}{m} \left[\mathbf{E}(\mathbf{x}_\alpha, t) + \frac{\mathbf{v}_\alpha}{c} \times \mathbf{B}(\mathbf{x}_\alpha, t)\right] + \mathbf{F}_L(\mathbf{x}_\alpha, t), \\ &\mathbf{F}_L = -\frac{1}{2\gamma_\alpha} \nabla \Phi_\alpha, \quad \gamma_\alpha^2 = 1 + |\mathbf{p}_\alpha|^2 + \Phi_\alpha, \\ &\frac{d\mathbf{x}_\alpha(t)}{dt} = \mathbf{v}_\alpha = \frac{c\mathbf{p}_\alpha}{\gamma_\alpha}, \end{aligned} \tag{13}$$

where all field variables have been projected on the particle guiding center following Eq. (12). In this framework, the averaged current density $\overline{\mathbf{J}}(\mathbf{x}, t)$ evolving on slow space–time scales, can be evaluated by:

$$\overline{\mathbf{J}}(\mathbf{x}, t) = \frac{q}{n_0 c} \sum_\alpha \mathbf{v}_\alpha(t) \hat{S}[\mathbf{x} - \mathbf{x}_\alpha(t)], \quad \mathbf{v}_\alpha = \frac{c\mathbf{p}_\alpha}{\gamma_\alpha}, \tag{14}$$

where the shape function $\hat{S}[\mathbf{x} - \mathbf{x}_\alpha(t)]$ now acts as distribution function for particle guiding centers. In the envelope equation (9), the $\chi(\mathbf{x}, t)$ function on the r.h.s is expressed by

$$\overline{\chi}(\mathbf{x}, t) = \frac{q^2}{n_0} \sum_\alpha \frac{\hat{S}[\mathbf{x} - \mathbf{x}_\alpha(t)]}{\gamma_\alpha}. \tag{15}$$

Recasting the oscillatory current component in the PGC formalism appears still an open problem, requiring elaborate perturbative analysis [4].

3. Implementing leapfrog integration scheme for envelope and wake field equations

The dispersion relation in Fourier modes $(\mathbf{k}, \omega)$ of Eq. (9) in linear approximation ($\chi \simeq 1$), is expressed by

$$\omega^2 + 2\omega_0\omega = c^2 \left(2k_0 k_z + k^2 + k_p^2\right), \tag{16}$$

where k_p is related to the plasma frequency as $\omega_p = ck_p$. Since in the envelope model $\omega - ck_z = \mathcal{O}(\varepsilon^2)$, relation (16) can be approximated by

$$\omega = ck_z + \frac{c}{2} \frac{k_\perp^2 + k_p^2}{k_0 + k_z} + \mathcal{O}\left(k_0 \varepsilon^4\right), \tag{17}$$

giving a group velocity $v_g = c + \mathcal{O}(\varepsilon^2)$ for right propagating modes $k_z > 0$

$$v_g = \frac{\partial\omega}{\partial k_z} = c \left[1 - \frac{1}{2} \frac{\widetilde{k}_\perp^2 + \widetilde{k}_p^2}{(1 + \widetilde{k}_z)^2}\right], \tag{18}$$

where $\widetilde{k} = k/k_0$ are the normalized wavenumbers.

In a Galilean frame moving at the speed of light (a *comoving system*), using coordinate transformations $(t, z) \to (\tau, \xi)$

$$\xi = z - ct, \quad \tau = t, \quad \partial_t = \partial_\tau - c\partial_\xi, \quad \partial_z = \partial_\xi, \tag{19}$$

the laser envelope equation (9), in the time ordering $\partial_\tau = \mathcal{O}(\omega_0 \varepsilon^2)$ with neglected second derivative $\partial_{\tau,\tau}$, reduces to

$$\left[ik_0 + \partial_\xi\right] \partial_\tau \hat{a} = -\frac{1}{2} \left[\nabla_\perp^2 - \omega_p^2 \chi\right] \hat{a} \tag{20}$$

which is the usually quoted form considered in analytical and numerical investigations, (see [3,5–8] and references therein). A main reason underlying this formulation is that a Galilean coordinate transformation induces a frequency shift $\omega \to \widetilde{\omega} = \omega - ck_z$, thus removing the highest frequency $\omega = ck_z$ in Eq. (17). The numerical integration of Eq. (20) is then expected to be free of dispersive effects related to the laser pulse advection.

However, to solve Eq. (20) for time derivative, the $\hat{M} \equiv [ik_0 + \partial_\xi]$ operator on the left has to be inverted and this poses severe limitations on implementation based on finite differences. In fact, the inverse operator

$$\hat{M}^{-1} = -\frac{ik_0 - \partial_\xi}{k_0^2 + \partial_{\xi,\xi}} \tag{21}$$

once discretized on a grid with cell size $\Delta\xi$, is singular at the Nyquist frequency $k_{max} = \pi/\Delta\xi \simeq k_0$, $\Delta\xi \simeq \lambda_0/2$. As a consequence, in explicit integration, grid resolution and Courant number must be severely bounded to assure stability. To overcome these limitations, in published works so far (see for example [9]), a semi-implicit integration scheme, typically a Crank–Nicolson integrator for the linear part, has been applied. This procedure requires inverting a fully 3*D* Laplacian discretized operator at each time step, with significant increase of computational complexity, also limiting an efficient parallel implementation.

In the cited works, differences arise on the way the envelope field solver relates to the wake field solver and to the plasma dynamical equations. In [3], envelope equation (20) is first integrated in a comoving (τ, ξ) coordinates and then advected back to the laboratory (t, z) coordinates, using $\partial_t + \partial_z = \partial_\tau$. This approach, once implemented by standard finite differences, reintroduces significant dispersive effects coming from the discretized advection operator. In work [6], laser and wakefield equations are all integrated on the comoving (τ, ξ) coordinate system. This entails, in particular, that the wakefield Maxwell equations have to be modified by a backward advection term and a streaming velocity $v_s = -c$ has to be added to the plasma particle motion. As a main consequence, strong anomalous Cherenkov effects are artificially produced, and additional computational costs are then required to control or reduce unphysical current driven instabilities.

3.1. Envelope field solver in the laboratory coordinate system

These arguments suggest that implementing the envelope wave equation directly on a laboratory coordinate system, as expressed in Eq. (9) with second time derivative operator retained, has to be preferred. In fact, Maxwell equation for the laser envelope can be integrated by stable explicit leapfrog schemes with no artificial restriction on CFL condition and on the grid resolution, thus allowing significant improvements in efficiency and simplicity of the implementation procedures. Also consistency arguments favoring this choice have to be considered, since Eq. (9) retains the basic (hyperbolic) structure of the wave equation for scalar fields and of the associated Maxwell equations for the laser driven wakefields. This entails, in particular, that the composite system of envelope, wakefields and particle equation of motion can be integrated on a same unitary numerical framework, as in fully kinetic PIC codes, using a second-order

leapfrog explicit integrator both for particles and fields, under the standard Courant number condition. To integrate Eq. (9) on a grid we use centered first and second finite differences to approximate time derivatives

$$\mathcal{D}_t\hat{a} = \frac{\hat{a}^{n+1} - \hat{a}^{n-1}}{2\Delta t}, \qquad \mathcal{D}_{t,t}\hat{a} = \frac{\hat{a}^{n+1} - 2\hat{a}^n + \hat{a}^{n-1}}{\Delta t^2}, \tag{22}$$

where index n denotes the time grid point $t^n = n\Delta t$ and Δt denotes the time step. Likewise, centered first and second finite differences on a (non staggered) grid $\mathbf{x}_g = (x_i, y_j, z_k)$ with cell sizes $(\Delta x, \Delta y, \Delta z)$ approximate space derivatives of the field $\hat{a}(x_i, y_j, z_k)$ discretized at integer index grid points:

$$\mathcal{D}_z\hat{a} = \frac{\hat{a}_{k+1} - \hat{a}_{k-1}}{2\Delta z}, \quad \mathcal{D}_{z,z}\hat{a} = \frac{\hat{a}_{k+1} - 2\hat{a}_k + \hat{a}_{k-1}}{\Delta z^2}, \qquad \mathcal{D}_{y,y}\hat{a} = \frac{\hat{a}_{j+1} - 2\hat{a}_j + \hat{a}_{j-1}}{\Delta y^2}, \quad \mathcal{D}_{x,x} = \frac{\hat{a}_{i+1} - 2\hat{a}_i + \hat{a}_{i-1}}{\Delta x^2}. \tag{23}$$

The Courant number $\sigma \leq 1$, relating Δt to the grid cell sizes is defined, as usual in numerical Maxwell equations, by

$$\sigma = \frac{c\Delta t}{\bar{h}\Delta z}, \quad \bar{h} = \frac{r}{\sqrt{2 + r^2}} \tag{24}$$

where $r = \Delta x/\Delta z = \Delta y/\Delta z$ is the ratio of the transverse to the longitudinal cell sizes ($\bar{h} = 1/\sqrt{3}$ for a uniform 3D grid).

In a laser-wakefield wave system, the discretized $\mathcal{D}_t + c\mathcal{D}_z$ operator entails dominant dispersive numerical errors with size $\mathcal{O}(\Delta t^2) - \mathcal{O}(\Delta z^2)$ given by the difference of second order truncation error in time and space, respectively. In long time integration of LWFA configurations, these errors shorten the dephasing length and affect then electron acceleration efficiency. A simple way to reduce these numerical effects is to modify finite difference operators along the z coordinate using a two-point enlarged stencils of grid points. In this way, still second-order, optimized numerical derivatives can be obtained, related to the standard two-point finite differences (23), by:

$$\mathcal{D}_z^{(o)} = \mathcal{D}_z\left[1 + \delta_1\Delta z^2\mathcal{D}_{z,z}\right], \qquad \mathcal{D}_{z,z}^{(o)} = \mathcal{D}_{z,z}\left[1 + \delta_2\Delta z^2\mathcal{D}_{z,z}\right], \tag{25}$$

where the free parameters (δ_1, δ_2) are chosen in a way to cancel out second order truncation errors of the space–time discretized advection operator. Using the dispersion relation expressed by numerical Fourier components, one obtains $\delta_1 = (\nu^2 - 1)/6 < 0$, and $\delta_2 = (\nu^2 - 1)/12 < 0$, where $\nu = \bar{h}\sigma = c\Delta t/\Delta z < 1$, (see Appendix A for a short derivation).

Modified finite differences is a standard issue in numerical analysis and has been widely used to reduce dispersive effects in FDTD for Maxwell wave equation (see [10]). In particular, a procedure similar to Eq. (25) has been introduced in [11], and, by more elaborate algorithm involving modified stencils also in transverse coordinates [12,13], especially designed to control anomalous Cherenkov effects of relativistic accelerated electron bunches. We point out, that the recipe here proposed involving only the longitudinal coordinate, takes fully advantage of the dominance of the advection operator in the envelope model, as documented in the numerical tests of Section 6.

In terms of finite difference operators, Eq. (9) is then expressed by

$$\left[\mathcal{D}_{t,t} - 2i\omega_0(\mathcal{D}_t + c\mathcal{D}_z) - c^2\mathcal{D}^2\right]\hat{a}^n(\mathbf{x}_g) = -\omega_p^2\chi(\mathbf{x}_g, t^n, |\hat{a}^n|)\hat{a}^n(\mathbf{x}_g), \tag{26}$$

where $\mathcal{D}^2 = \mathcal{D}_{z,z} + \mathcal{D}_\perp^2$ denotes the $3D$ numerical Laplacian operator and $\mathcal{D}_\perp^2 = \sum_{s=x,y}\mathcal{D}_{s,s}$. In code implementation, either standard (*i.e.* Eq. (23)) or optimized (*i.e.* Eq. (25)) finite differences along the $z-$coordinate can be activated.

For given $[\hat{a}^n(\mathbf{x}_g), \hat{a}^{n-1}(\mathbf{x}_g)]$ field data at time level $t^n = n\Delta t$ and $t^{n-1} = t^n - \Delta t$, the one step update of Eq. (26) is implemented by first evaluating at the current time level t^n the source term

$$\hat{S}[\hat{a}] = \left[2ik_0\mathcal{D}_z + \mathcal{D}^2 - \omega_p^2\chi(\mathbf{x}_g, t^n)\right]\hat{a}^n(\mathbf{x}_g) \tag{27}$$

and then by solving in explicit form for the updated field data:

$$\hat{a}^{n+1} - i\eta\hat{a}^{n+1} = \widetilde{F}[\hat{a}], \qquad \widetilde{F}[a] = \Delta t^2\hat{S}[\hat{a}] + 2\hat{a}^n - \hat{a}^{n-1} - i\eta\hat{a}^{n-1}, \tag{28}$$

where $\eta = \omega_0\Delta t$. Finally, by separating real and imaginary components $\hat{a} = (a_R, a_I)$, the solution for the updated variables $(a_R, a_I)^{n+1}$ is evaluated by

$$a_R^{n+1} = \frac{F_R - \eta F_I}{1 + \eta^2}, \quad a_I^{n+1} = \frac{F_I + \eta F_R}{1 + \eta^2}. \tag{29}$$

where the source term components are given by

$$\widetilde{F}_R = \Delta t^2\hat{S}_R + 2a_R^n - a_R^{n-1} + \eta a_I^{n-1}, \quad \widetilde{F}_I = \Delta t^2\hat{S}_I + 2a_I^n - a_I^{n-1} - \eta a_R^{n-1}. \tag{30}$$

3.2. Implementation of leapfrog Maxwell solver for driven wakefield

By representing the $(\mathbf{E}, \mathbf{B}, \mathbf{J})$ fields on the standard Yee grid, the leapfrog integrator of Maxwell equations for wakefield equation (4) is expressed by

$$[\mathcal{D}_t\mathbf{B}]^n = -c\mathcal{D} \times \mathbf{E}^n, \qquad [\mathcal{D}_t\mathbf{E}]^{n+1/2} = c\mathcal{D} \times \mathbf{B}^{n+1/2} - \omega_p\mathbf{J}^{n+1/2} \tag{31}$$

where, as usual in FDTD framework, finite differences in space and time are evaluated at staggered grid points with respect to the collocation of the derived variables.

Since also driven wakefields are advection dominated, dispersive numerical errors can be reduced following the same procedure adopted for the envelope field solver. In the Yee staggered grid, optimized finite differences along the $z-$coordinate are now defined by

$$\mathcal{D}_z^{(o)} = \mathcal{D}_z\left[1 + \delta_3\Delta z^2\mathcal{D}_{z,z}\right], \quad \delta_3 = \frac{\nu^2 - 1}{24}, \tag{32}$$

and are then applied to the proper components of both the $(\mathcal{D}\times\mathbf{E})$ and $(\mathcal{D} \times \mathbf{B})$ vector operators.

4. Leapfrog integration of equation of motion of PIC particles

4.1. Boris pusher for particle momentum update

In a leapfrog integration scheme of Eq. (13), the one-step update $\mathbf{p}_\alpha^{n-1/2} \to \mathbf{p}_\alpha^{n+1/2}$ of particle momentum discretized on the staggered time grid, is expressed by

$$\mathbf{p}_\alpha^{n+1/2} = \mathbf{p}_\alpha^{n-1/2} + \Delta t\left[\frac{q\omega_p}{m}\left(\mathbf{E}_\alpha^n + \frac{\mathbf{v}_\alpha^n}{c} \times \mathbf{B}_\alpha^n\right) - \frac{1}{2\gamma_\alpha^n}\nabla\Phi_\alpha^n\right]. \tag{33}$$

On the right side, grid defined fields $[\mathbf{E}^n(\mathbf{x}_g), \mathbf{B}^n(\mathbf{x}_g)]$ and $[\Phi^n(\mathbf{x}_g), \nabla\Phi^n(\mathbf{x}_g)]$ are evaluated at the current time level t^n by the previous $t^{n-1} \to t^n$ update expressed in Eqs. (29) and (31), and then assigned to each particle position $\mathbf{x}_\alpha^n$ using splines $\hat{S}_{\mathbf{x}_g}[\mathbf{x}_g - \mathbf{x}_\alpha^n]$ of some order, as routinely defined in the PIC method. To preserve the leapfrog scheme structure and accuracy, all time centered variables, $\mathbf{u}^n \equiv [\mathbf{E}, \mathbf{B}, \Phi, \mathbf{x}_\alpha, \mathbf{v}_\alpha]^n$ on the right hand side are required to be at least second order approximations, $\mathbf{u}^n = \mathbf{u}(t^n) + \mathcal{O}(\Delta t^2)$. To that purpose, in the Boris scheme [14], the

particle velocity is defined by using mid-point rule for centered momentum,

$$\mathbf{v}_\alpha^n = \frac{c\mathbf{p}_\alpha^n}{\gamma_\alpha^n}, \quad \mathbf{p}_\alpha^n = \frac{\mathbf{p}_\alpha^{n+1/2} + \mathbf{p}_\alpha^{n-1/2}}{2}, \\ \gamma_\alpha^n = \left[1 + |\mathbf{p}_\alpha^n|^2 + \Phi_\alpha^n\right]^{1/2}, \tag{34}$$

but other choices have been proposed as well [15]. In terms of the unknown variables $\mathbf{p} \equiv \mathbf{p}_\alpha^n$, and $\gamma \equiv \gamma^n(|\mathbf{p}|^2)$ as defined in Eq. (34), the momentum equation (33) (particle α index omitted for brevity) can be reformulated as a fully implicit algebraic system

$$\mathbf{p} = \mathbf{p}^{n-1/2} + (\widetilde{\mathbf{E}} - \widetilde{\mathbf{F}}/\gamma) + \mathbf{p} \times \widetilde{\mathbf{B}}/\gamma \tag{35}$$

with $\mathcal{O}(\Delta t)$ coefficients given by

$$\widetilde{\mathbf{E}} \equiv \Delta t \frac{q\omega_p}{2m}\mathbf{E}^n, \quad \widetilde{\mathbf{B}} \equiv \Delta t \frac{q\omega_p}{2m}\mathbf{B}^n, \quad \widetilde{\mathbf{F}} = \frac{\Delta t}{4}\nabla\Phi^n. \tag{36}$$

The Boris procedure to solve (35) is based on the following two main computational steps:

(i) the exact γ function is reduced to explicit form, by a Taylor expansion to a $\mathcal{O}(\Delta t^2)$ approximation using the same equation (35);
(ii) the term related to the magnetic field is evaluated in exact explicit form using standard vector algebra (usually interpreted as magnetic rotation).

The main change to be applied in the envelope model refers to task (*i*), of course, for the presence on the $1/\gamma$ factor in the ponderomotive force. By replacing $\mathbf{p} \to \mathbf{p}^{n-1/2} + (\widetilde{\mathbf{E}} - \widetilde{\mathbf{F}}/\gamma) + \mathcal{O}(\Delta t^2)$ in the γ definition equation (34), the approximated $\widetilde{\gamma}$ variable is solution of the cubic equation

$$\widetilde{\gamma}^2 = \left[\gamma_0^2 + 2(\widetilde{\mathbf{E}} - \frac{\widetilde{\mathbf{F}}}{\widetilde{\gamma}}) \cdot \mathbf{p}^{n-1/2}\right], \quad \gamma_0^2 = \left(1 + \Phi^n + |\mathbf{p}^{n-1/2}|^2\right), \tag{37}$$

which reduces consistently to the approximation in standard PIC model when $\Phi = 0$, (*i.e.* $\widetilde{\mathbf{F}} = 0$).

By replacing $\gamma \to \widetilde{\gamma}$, the momentum equation (35) can now be solved in explicit form using the Boris procedure indicated in step (*ii*):

$$\mathbf{p} = \frac{1}{1 + |\mathbf{h}|^2}\left[\mathbf{u} + \mathbf{u} \times \mathbf{h} + \mathbf{h}(\mathbf{u} \cdot \mathbf{h})\right], \\ \mathbf{p}^{n+1/2} = 2\mathbf{p} - \mathbf{p}^{n-1/2}, \tag{38}$$

where $\mathbf{u} = \mathbf{p}^{n-1/2} + \widetilde{\mathbf{E}} - \widetilde{\mathbf{F}}/\widetilde{\gamma}, \quad \mathbf{h} = \widetilde{\mathbf{B}}/\widetilde{\gamma}$.

4.2. Update of particle position in envelope model

The leapfrog scheme to update particle position, is given by

$$\mathbf{x}_\alpha^{n+1} = \mathbf{x}_\alpha^n + \Delta t \mathbf{v}_\alpha^{n+1/2}, \quad \mathbf{v}_\alpha^{n+1/2} = \frac{c\mathbf{p}_\alpha^{n+1/2}}{\gamma_\alpha^{n+1/2}}, \\ \gamma_\alpha^{n+1/2} = \left(1 + \left|\mathbf{p}_\alpha^{n+1/2}\right|^2 + \Phi_\alpha^{n+1/2}\right)^{1/2}, \tag{39}$$

where now the ponderomotive potential $\Phi_\alpha^{n+1/2} = \Phi^{n+1/2}(\mathbf{x}_\alpha^{n+1/2})$ has an implicit dependence on the particle position since $\mathbf{x}_\alpha^{n+1/2} = (\mathbf{x}_\alpha^{n+1} + \mathbf{x}_\alpha^n)/2$. To evaluate Eq. (39) in closed explicit form, still preserving the leapfrog structure and accuracy, we follow the approach first suggested in [16]. In the shorthand notation $\mathbf{p} \equiv \mathbf{p}^{n+1/2}$, $\Phi \equiv \Phi^{n+1/2}$, $\gamma \equiv \gamma^{n+1/2}$ the implicit $\Phi(\mathbf{x}^{n+1/2})$ function can be linearized by a first order Taylor expansion

$$\Phi(\mathbf{x}^{n+1/2}) = \Phi\left(\mathbf{x}^n\right) + \delta\mathbf{x} \cdot \nabla\Phi\left(\mathbf{x}^n\right), \\ \delta\mathbf{x} = \mathbf{x}^{n+1/2} - \mathbf{x}^n = \frac{\mathbf{x}^{n+1} - \mathbf{x}^n}{2}, \tag{40}$$

where the gradient operator can act on the $\mathbf{x}_g$ argument of the shape function $\hat{S}_{\mathbf{x}_g}[\mathbf{x}_g - \mathbf{x}]$ or of the $\Phi(\mathbf{x}_g)$ field. The γ function of Eq. (35) can be evaluated in explicit form by solving the cubic equation (see [16])

$$\widetilde{\gamma}^3 = \widetilde{\gamma}\gamma_0^2 + \frac{\Delta t}{2}\left(\mathbf{p} \cdot \nabla\Phi\left(\mathbf{x}^n\right)\right), \quad \gamma_0^2 = 1 + |\mathbf{p}|^2 + \Phi\left(\mathbf{x}^n\right), \tag{41}$$

or by a simpler, still second order, explicit approximation

$$\widetilde{\gamma}^{-1} = \frac{1}{\gamma_0}\left[1 - \frac{\Delta t}{4\gamma_0^3}\left(\mathbf{p} \cdot \nabla\Phi\right)\right]. \tag{42}$$

In this way, the update of the particle position takes finally the explicit form:

$$\mathbf{x}_\alpha^{n+1} = \mathbf{x}_\alpha^n + \Delta t \mathbf{v}_\alpha^{n+1/2}, \quad \mathbf{v}_\alpha^{n+1/2} \equiv \widetilde{\gamma}^{-1} c\mathbf{p}_\alpha^{n+1/2}. \tag{43}$$

4.3. The overall integration one-step cycle of the envelope model

At the end of the momentum update step, Eq. (38), the source term $\chi^n\left(\mathbf{x}_g, t^n, \left|\hat{a}^n\right|\right)$ needed to update the complex envelope field in Eq. (29), is evaluated using the particle $\widetilde{\gamma}(\mathbf{x}_\alpha^n)$ function defined in (37), by

$$\chi^n(\mathbf{x}_g) = \frac{q^2}{n_0}\sum_\alpha \hat{S}\left(\mathbf{x}_g - \mathbf{x}_\alpha^n\right)\left[\widetilde{\gamma}\left(\mathbf{x}_\alpha^n\right)\right]^{-1}. \tag{44}$$

By mid-point rule, the $\Phi^{n+1/2}(\mathbf{x}_g)$ field is then computed, to update particle positions $\mathbf{x}_\alpha^{n+1}$ and velocities $\mathbf{v}_\alpha^{n+1/2}$ by Eq. (43).

Finally, the current density $\mathbf{J}^{n+1/2}(\mathbf{x}_g)$ in the Maxwell equation for wakefield, (31), is then constructed using particle positions and velocity by

$$\mathbf{J}^{n+1/2}(\mathbf{x}_g) = \frac{q}{cn_0}\sum_\alpha \hat{S}_{\mathbf{x}_g}[\mathbf{x}_g - \mathbf{x}_\alpha^{n+1/2}]\mathbf{v}_\alpha^{n+1/2} \tag{45}$$

where shape function $\hat{S}[\mathbf{x} - \mathbf{x}_\alpha]$ has to be designed in a way to enforce the discretized continuity equation for local charge conservation [17].

In the following, the overall numerical procedure encoding one-step cycle to update particle coordinates, as detailed above, the laser envelope field, Eq. (29) and wakefield solver, (31), will be denoted as ENV/PIC. In the following Section 6, we present a numerical documentation to support error analysis of the proposed schemes.

We have presented in some details the ENV/PIC implementation also because only few works are available on the subject. In work [5], the γ^n function used to implement the Boris algorithm is evaluated by an independent first order integration scheme. In work [3], the Boris procedure to update particle momentum is never explicitly documented, whereas the update of particle position is implemented using a sequence of first order Euler integrations, like a predictor-correction scheme. Moreover, since no error analysis nor convergence test for particle motion has been presented, it is quite difficult to make useful comparisons and cross-checking.

5. Eulerian integration of laser–plasma dynamics in envelope model

Even if the ENV/PIC implementation assures significant saving of computational resources with respect to standard fully kinetic PIC codes (but a precise estimate of speed-up depends crucially

on the chosen number of particle per cell), long time integration of plasma dynamics using particles is still challenging and time consuming. A direct numerical integration of plasma momentum-density equations in Eulerian variables equation (11), coupled to Eqs. (29) and (31), can offer a promising and faster alternative to the ENV/PIC schemes, applicable for several LWFA regimes. In fact, the computational complexity of a discretized fluid model can be evaluated to be roughly equivalent to the corresponding PIC model containing just one particle per cell.

The momentum-density system of Eqs. (11) has the form of a relativistic, pressureless Euler equation with a non-linear forcing coupling momentum advection to the Maxwell field equations. It is clearly challenging since no rigorous numerical analysis results are available. However, accurate and stable integration schemes can still be constructed by taking into account the computational experience in the ordinary Eulerian system for collisional gas dynamics.

A straightforward application of a leapfrog scheme to system (11) using centered numerical derivatives in space and time fails to preserve monotonicity in wave profile (Gibbs pathology) even for modest non-linear steepening, finally leading to numerical instabilities. To prevent or limit this pathology, non-oscillatory (or monotonicity preserving) upwind scheme has been designed and widely applied to simulate compressible fluid dynamics [18]. The implementation we propose here is based on the second order, one-step Adams–Bashforth (*AB*) scheme for time integration and on second-order Weighted Essentially Non-Oscillatory *WENO2* upwind scheme [19] to evaluate space derivatives. We have chosen *AB* scheme essentially because it is one step and it works as a "modified" leapfrog scheme, and so can be naturally associated to the Maxwell field solvers, thus assuring a unitary computational frame-work for the overall system.

By representing the plasma fluid-dynamics equation (11) in terms of the four-dimensional arrays of fluid variables $u \equiv [\mathbf{p}, n]^T$ (overbar symbols omitted for brevity), one has

$$\partial_t u(\mathbf{x}, t) = F[u, \mathbf{x}, t], \tag{46}$$

where the vector $F \equiv [F_{\mathbf{p}}, F_n]$ has components

$$\begin{aligned} F_{\mathbf{p}} &= -(\mathbf{v}\cdot\nabla\mathbf{p}) + \mathbf{F}_{tot}, \\ F_n &= -\nabla\cdot(n\mathbf{v}), \end{aligned} \tag{47}$$

in which $\mathbf{v} = c\mathbf{p}/\gamma$ and the total Lorentz force acting on a fluid element is given by

$$\mathbf{F}_{tot}[\mathbf{x}, \mathbf{p}, t] = \frac{q\omega_p}{m}\left[\mathbf{E} + \frac{\mathbf{p}}{\gamma}\times\mathbf{B}\right] - \frac{1}{2\gamma}\nabla\Phi, \quad \Phi = \frac{q^2|\hat{a}|^2}{2m^2}, \tag{48}$$

with $\gamma(\mathbf{p}, \mathbf{x}, t) = \left[1 + |\mathbf{p}|^2 + \Phi\right]^{1/2}$. Here we choose to integrate momentum equation using a non-conservative advection operator $\mathbf{F}_{adv} = (\mathbf{v}\cdot\nabla)\mathbf{p}$, because, in this form, Eq. (46) decouples from the density equation and implementation turns out to be simpler than using the $[n\mathbf{p}]$ momentum variable. We have also implemented momentum equation using a conservative advection flux, but no significant differences between the two implementations have been noticed. On the other hand, there are no general reasons to use conservative advection, since plasma momentum equation has not a general conservation form.

Once discretized on a space–time $\left[\mathbf{x}_g, t^n\right]$ grid, the *AB* update of momentum-density variable $u^n(\mathbf{x}_g)$ is expressed by

$$u^{n+1} = u^n + \frac{\Delta t}{2}\left[3F^n - F^{n-1}\right], \tag{49}$$

where $F^n \equiv F\left[u^n, \mathbf{x}_g, t^n\right]$. We notice that the update in Eq. (49) is in fact one-step, since F^{n-1} can be evaluated only once at a previous $t^{n-1} \to t^n$ integration step and then stored. For linear system, the resulting approximation for time derivative results to be

$$\mathcal{D}_t u = \frac{u^{n+1} - u^n}{\Delta t} = \frac{du}{dt} + c_1\Delta t^2\left[\frac{d^3u}{dt^3}\right] + c_2\Delta t^3\left[\frac{d^4u}{dt^4}\right] \tag{50}$$

showing that the leading order approximation has a dispersive character, as in the associated leapfrog integrator for the envelope and wake field equations, plus a higher order $\mathcal{O}(\Delta t^3)$ dissipative error to balance dissipative numerical errors coming from upwind numerical space derivatives.

Upwind schemes based on the WENO reconstruction procedures offer the following advantages: (i) they assure uniform second (or even higher) order approximation even of steep gradients, and (ii) they provide a robust and accurate numerical approximation of space derivatives, even for non conservative fluid-dynamics systems [20,21].

The numerical procedure encoding the composite [*AB* − *WENO2*] scheme for Eq. (46), coupled to field solvers in Eqs. (29) and (31) is here denoted as ENV/Fluid. It turns out to be stable and accurate even for modest grid resolution, for a wide class of problems, covering linear and non-linear conditions, as documented below in the preliminary tests we have considered. For strongly non-linear regimes, when a high intensity laser generates a bubble in the plasma density, a cold-fluid approximation is no longer appropriate.

The ENV/Fluid scheme, where it applies, can fully replace ENV/PIC scheme only in the study of time evolution, structure and propagation properties of the laser-driven wakefield system. When kinetic effects are of interest, like injection and acceleration of electron bunches in a wake field, the ENV/Fluid is no longer appropriate, of course. However, taking advantage of the unitary computational frame-work here proposed, it can still be used in association with the ENV/PIC scheme in a composite hybrid fluid-kinetic computational framework.

6. Numerical benchmark of the envelope approximation

In this section, we test the accuracy of the modified Boris pusher, of the laser envelope solver and the fluid scheme we have introduced in this work. Laser–plasma interaction is in general a strongly nonlinear problem and analytical expressions for the time evolved quantities are only rarely available. Thus, in order to propose a robust benchmark, we first check the correctness of the single particle motion and of laser evolution *in-vacuum*, where it is possible to compare directly the results with the theory, then we investigate the fully nonlinear laser–plasma interaction.

At the current time, we always initialize a laser pulse as the product of a Gaussian transverse profile of given waist at focus w_0 and a Gaussian longitudinal profile with pulse *intensity* duration (Full Width at Half Maximum) τ_{fwhm}, so that $\hat{a}(\mathbf{x}) = a^T(\mathbf{x})a^L(\mathbf{x})$. In particular, the transverse profile is given by

$$a^T(z, r) = \exp\left[-\frac{r^2}{w(z)^2}\right], \quad r^2 = x^2 + y^2, \tag{51}$$

where $w(z)$ is the usual expression for the waist of a Gaussian pulse focalized in $z = z_f$ with a Rayleigh length Z_{Ra}, $w(z) = w_0\sqrt{1+\tilde{z}^2}$ and $\tilde{z} = (z - z_f)/Z_{Ra}$, while the longitudinal one is

$$a^L(z, r) = \frac{a_0}{\sqrt{1+\tilde{z}^2}}\exp(i\varphi)\exp\left[-\frac{(z-z_f)^2}{L_z^2}\right], \tag{52}$$

where, following [2], $\varphi = \arctan\left(\tilde{z}\right) - \tilde{z}r^2/w(z)^2$ and L_z is related to the characteristic length $c\tau_{fwhm}$ via $L_z = c\tau_{fwhm}/\sqrt{2\log(2)}$. From now on, our simulations will refer to a laser pulse of wavelength $\lambda_0 = 0.8\ \mu$m propagating in a 3*D* cartesian geometry.

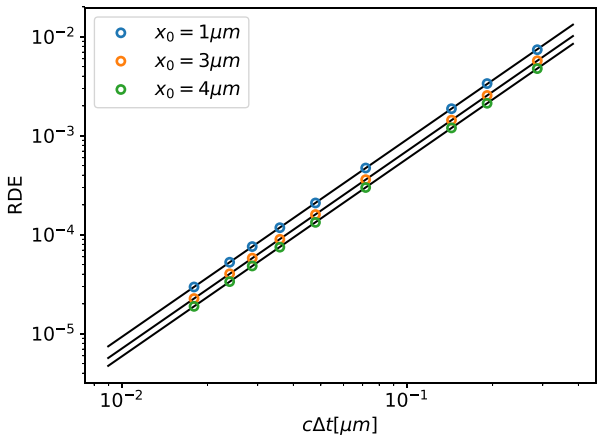

Fig. 1. Relative discretization error of the transverse component of the particle position in function of the resolution (colors online).

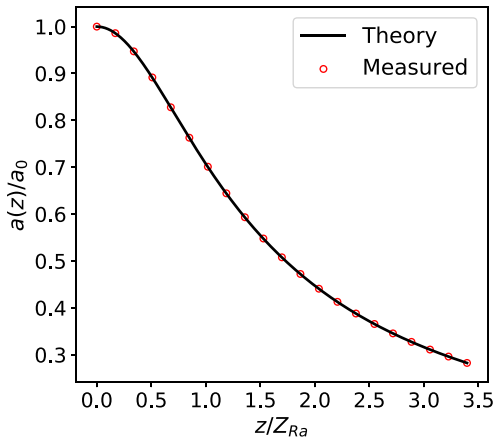

Fig. 2. We show (red circles) the simulated peak amplitude as a function of the propagation distance, for a diffracting laser propagating in vacuum up to a distance of 3000 μm.

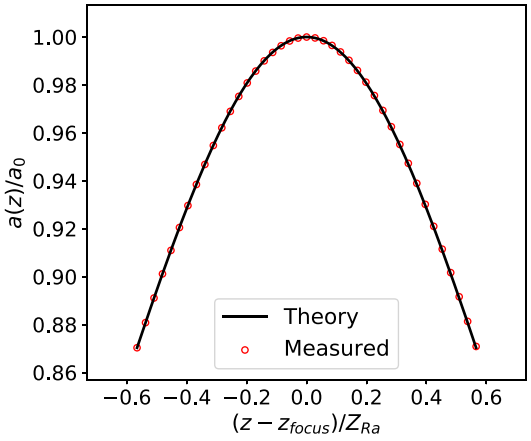

Fig. 3. A laser pulse in vacuum focalizes and then defocalizes so it can be seen that the error is low enough for the initial condition to be recovered.

6.1. Particle pusher quadratic convergence

We show a grid convergence test performed on particle trajectories interacting with a laser field. In Section 4, we have presented a modified Boris pusher that takes into account the ponderomotive force of the laser expressed in the envelope approximation. Error analysis shows that a second order convergence is expected. To perform this check, we initialized some test particles, distributed with initial zero initial velocity on a plane perpendicular to the laser propagation axis, and four broad laser pulses in vacuum, all of them aligned, that interact via Eq. (13) with the particles. We have chosen a nontrivial field to enhance the effect of the ponderomotive force on the particles. For any test particle, the test has been performed by measuring the final position in function of the resolution and then derived the expected value via a Richardson extrapolation. The Relative Discretization Error (RDE) accumulated along the trajectory scales exactly as $RDE \sim \Delta t^2$, as it is shown in Fig. 1, where every line in LogLog scale has a slope $p = 2$.

6.2. Tests in vacuum

A propagating laser pulse diffracts due to its finite width, that is while moving away from its focal position, *i.e.* defocalizing, the amplitude decreases and the spot size increases to preserve the total energy. In particular, in a linear medium, such as vacuum, it is possible to obtain an analytical expression for the laser pulse evolution by directly solving the electromagnetic wave equation in the paraxial approximation. Rayleigh diffraction thus represents a solid numerical benchmark for any electromagnetic wave solver. Given the amplitude at focus a_0 as the initial condition, the amplitude evolution in time is expressed as $a(t) = a_0\left(1 + \tilde{z}^2\right)$.

In Fig. 2, we study the evolution of the peak amplitude for a $\tau_{fwhm} = 75$ fs and $w_0 = 15$ μm laser pulse starting at the focal point and propagating for 3000 μm, which corresponds to 3.5 Rayleigh lengths. In black, we report the analytical peak amplitude evolution in the paraxial approximation. The measured peak amplitude of the simulated laser pulse during its propagation, represented with the red circles, shows perfect agreement with the theoretical expectations.

The same laser pulse can be initialized before its focal point so that its amplitude has to increase to reach its maximum value exactly at focus. We let the pulse propagate for twice the initial distance from the focus, because, since the electromagnetic field evolution is symmetric, we expect at the end to recover the initial conditions. In a comoving reference frame, longitudinal and transverse laser profiles must therefore overlap after the diffraction process but in numerical simulations, temporal symmetry can only be achieved if numerical dissipation, affecting the total energy, and dispersion, affecting the propagation speed, are kept very low. In particular, in a leapfrog integration scheme, only dispersive error is expected. In Fig. 3, is shown the peak amplitude evolution before and after focusing. In Figs. 4(a) and 4(b), the longitudinal and transverse profiles are overlapped, to verify that the integration scheme presents very low dispersion over long distances. Since the results agree with the expected values, time reversibility is assured. These simulations were run with a resolution of $\lambda_0/\Delta z = 12.5$, with $\Delta y = \Delta x = 8.99\Delta z$ and a CFL $\sigma = 0.7$.

In Section 3, we presented an optimized numerical integration scheme to reduce the dispersive effects affecting wave propagation speed. In the following, we study the envelope solver dispersive error in function of the resolution for a laser pulse with $\tau_{fwhm} = 75$ fs, $w_0 = 30$ μm, $a_0 = 1$ propagating in vacuum, evaluating dispersive effects measured either with the standard FDTD centered scheme or with the optimized one defined in Eq. (25). Then, we compare the outcomes with the results obtained simulating the same laser pulse with a standard PIC code, that is when laser oscillations are retained. It is known that to well reproduce group velocities in a PIC scheme, the highest frequency (*i.e.* laser frequency) has to be well resolved.

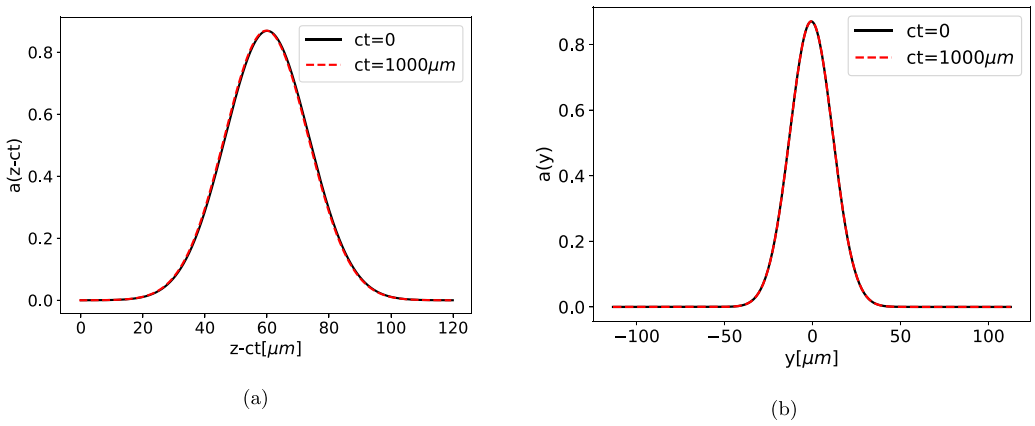

Fig. 4. Superposition of the longitudinal (Fig. a) and transverse (Fig. b) laser profile at the beginning and at the end of the simulation.

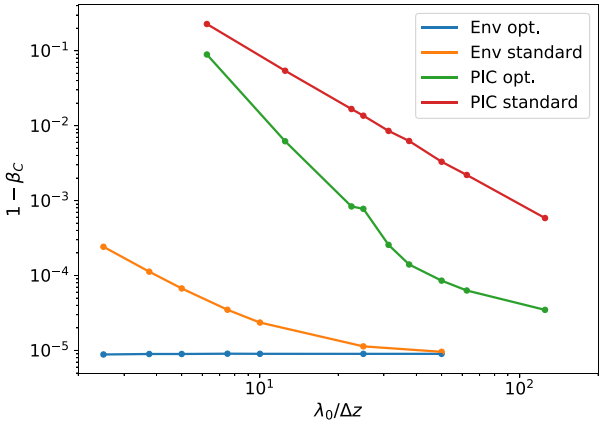

Fig. 5. Comparison between the phase velocities of the laser pulse centroid when it is propagating in vacuum in various computational configurations. In particular, in the ENV/PIC optimized case, $1-\beta_c$ is lower than the measurement error for every resolution we considered (colors online).

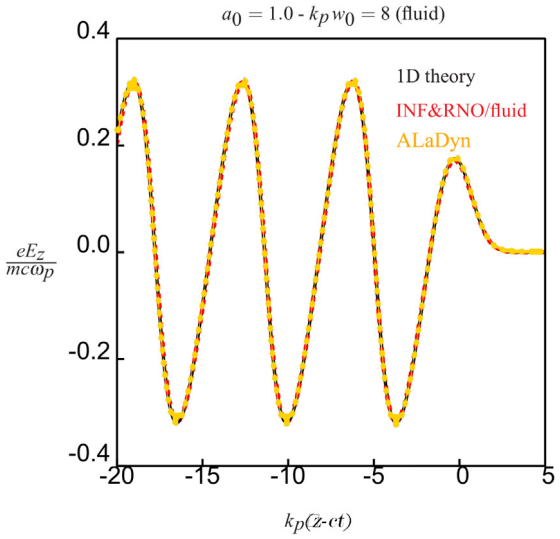

Fig. 6. Wakefield generated by a 1D configuration. We compare it with the theoretical result given by the 1D quasi-static nonlinear theory (black) and the one obtained by INF&RNO/Fluid (colors online).

For a laser pulse propagating in vacuum, we define the centroid position as

$$z_c(t) = \frac{\int z|\hat{a}(\mathbf{x},t)|^2 d\mathbf{x}}{\int |\hat{a}(\mathbf{x},t)|^2 d\mathbf{x}} = \frac{\sum_{\mathbf{x}_g} z_i \hat{a}^n_{i,j,k}}{\sum_{\mathbf{x}_g} \hat{a}^n_{i,j,k}}, \tag{53}$$

where the sum is extended on all the computational grids, then we numerically derive $z_c(t)$ to get the group velocity. For the two computational frameworks considered (PIC and ENV/PIC), $1-\beta_c = 1-v_g/c$ for both the standard centered and the optimized differentiation schemes are represented in Fig. 5. In this run, while varying Δz, we fixed a uniform transverse grid (that is $\Delta y = \Delta x = \Delta z$) and $\sigma = 0.8$. To obtain comparable errors in the PIC scheme, resolution must be increased by at least an order of magnitude, depending on the problem, thus assuring the strong time saving property of the envelope solver. We point out that for optimized derivative in the ENV scheme, discretization error is well below the measurement one, induced by Eq. (53).

6.3. Nonlinear laser–plasma interaction

For a robust test in the nonlinear regime, we follow the "Test 3" reported in [6] where a comparison of the wakefield generated by INF&RNO/Fluid (a fluid 2D cylindrical code based on the envelope description, see [6,9]) and the 1D (broad pulse) analytical nonlinear theory is presented. Performing the simulation with the same parameters, we obtain perfectly overlapping results with the INF&RNO/Fluid and the analytical value, as shown in Fig. 6, where the propagation distance has been normalized to the plasma wavenumber. Such result shows the correctness of the particle motion for particles self-consistently coupled to the wakefield.

In LWFA experiments, where the acceleration distance can be of the order of many Rayleigh lengths, guiding methods have been proposed to avoid early laser diffractions. In particular, a Gaussian pulse can be matched in a parabolic density plasma channel, where the Rayleigh diffraction is balanced by the focalizing effect due to the medium, and therefore no significant changes in the longitudinal and transverse profile are present for propagation distances $z \gg Z_{Ray}$. In [7,22], a semianalytical model is developed to compute the exact propagation velocity of a laser pulse in a matched plasma channel of given density profile, with $a_0 < 1$. For accurate simulations of LWFA regimes, it is crucial that group and phase laser velocity are well reproduced by the laser solver even when the pulse interacts with a nonlinear medium for long distances. To check the stability of the proposed solver, a laser pulse with $a_0 = 0.1$, $w_0 = 8.9$ μm and $\tau_{fwhm} = 21.3$ fs is shot through a matched plasma channel with a density on axis $n_0 = 4.25 \times 10^{18}$ cm^{-3}, then we compare the results

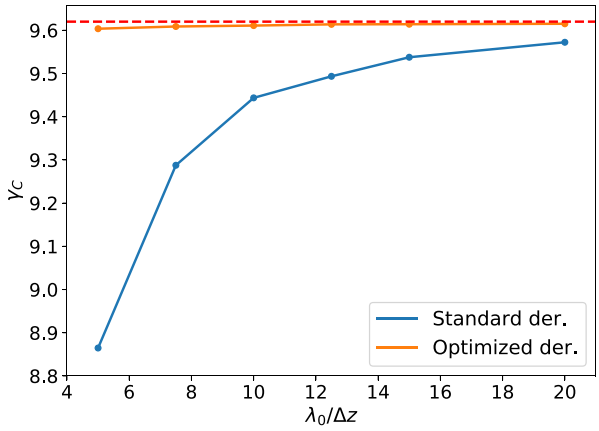

Fig. 7. Relativistic factor γ_c concerning the propagation of a Gaussian laser pulse in a matched plasma channel in function of the resolution. The semianalytical value is shown in red (colors online).

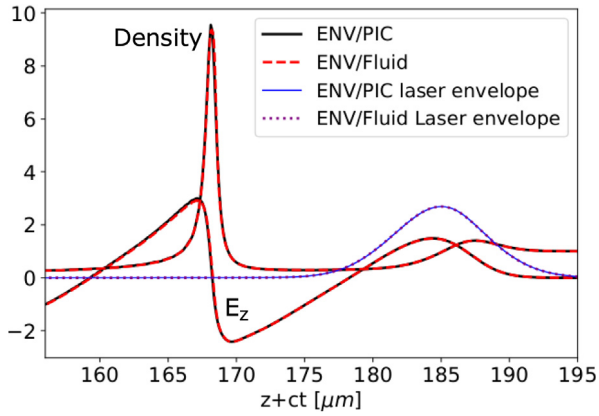

Fig. 8. We show a comparison after $ct = 150$ μm of propagation between an ENV/PIC and an ENV/Fluid simulation in a mildly nonlinear regime, where we expect the fluid model to hold.

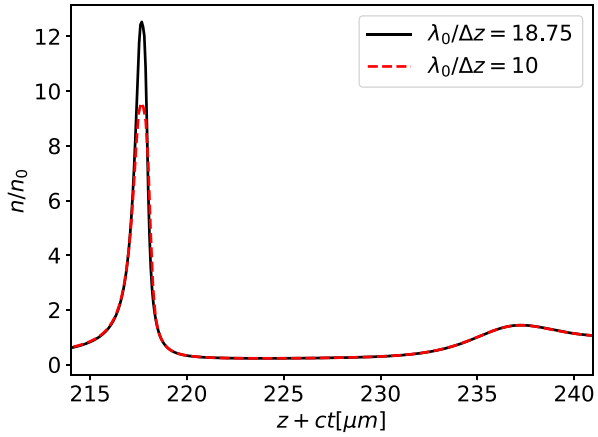

Fig. 9. Dissipation effects in density relative to the AB-WENO2 scheme after $ct = 200\mu m$ of laser propagation in a uniform plasma.

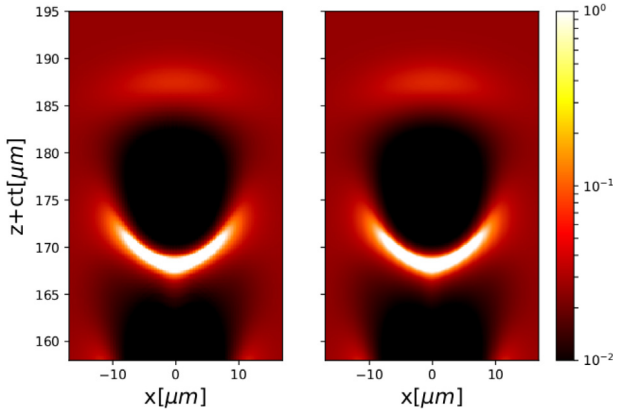

Fig. 10. Log density maps relative to the simulation presented in Fig. 8 obtained in the ENV/PIC (left) and in the ENV/Fluid (right) (colors online).

of the measured group velocity obtained with the optimized and standard numerical derivatives. With this choice of the laser and plasma parameters, the expected value for the relativistic factor associated with the laser centroid is $\gamma_c = 9.63$. In Fig. 7 it can be seen that the optimized algorithm shows much faster than quadratic convergence to the exact value even for modest resolutions.

6.4. Benchmark of the Eulerian integrator for the plasma fluid density

It is expected the fluid model to precisely reproduces the same fields as the PIC scheme away from the plasma bubble regime, where wavebreaking happens and the Lorentz–Maxwell system of equations does not provide an adequate description. Such regime is in fact limited by the theoretical foundation of the plasma fluid description and by the practical need to deal with the typical discontinuities that characterize the strongly nonlinear laser plasma interaction. In fact, one should resort to very specific integration schemes, able to avoid instabilities and to enforce the numerical density positivity in the continuity equation. For this reason, simulation of an extremely nonlinear regime in a fluid framework is still a theoretical and computational open problem, even though some comparisons have been provided in [23,24] that show some disagreements in the wakefield generation with respect to a fully kinetic code. In Fig. 8, we report the comparison between an ENV/PIC and an ENV/Fluid simulations when considering the nonlinear laser plasma interaction generated by the propagation of a nonlinear laser pulse with $a_0 = 2.5$, $w_0 = 12.7$ μm and $\tau_{fwhm} = 20$ fs in a uniform plasma of density $n_0 = 4.25 \times 10^{18}$ cm^{-3}. The ENV/PIC simulation was run with a resolution $\lambda_0/\Delta z = 10$, while in this configuration we needed $\lambda_0/\Delta z = 18.75$ with $\sigma = 0.4$ in the ENV/Fluid to reach the perfect agreement. For lower resolutions in the ENV/Fluid configuration, the numerical diffusion induced by discretization errors of the upwind scheme, generated high dissipation of the density profile peak amplitude after 200 μm of propagation. The dissipative effect is quite sensitive to the adopted resolution, as shown in Fig. 9 where the same ENV/Fluid configuration is run with a resolution $\lambda_0/\Delta z = 10$. At the end, an overall comparison based on empirical observation, is shown in Fig. 10, where the 2D density maps relative to the ENV/PIC and the ENV/Fluid simulations with the same parameters as in Fig. 8 present a good agreement also for the transverse density distribution.

7. Conclusions

We have presented in detail integration schemes and implementation procedures for numerical simulation of the envelope model for LWFA regimes. The field solver for laser propagation has been implemented in the laboratory coordinate system in 3D cartesian geometry. This unconventional approach allows, in particular, to integrate the exact (to within the model) wave equation

for the envelope field by an explicit leapfrog scheme working under the same CFL stability condition as in the related Maxwell solver for wakefield and PIC particles motion. Since in the physical regimes under consideration, laser-wakefield propagation is advection dominated, that is time evolution is slow, quasi-static in the limit, in a comoving system, numerical space derivatives along the propagation direction have been properly designed to reduce dispersion errors coming from discretized wave operators. This strongly improves grid convergence to the envelope model theoretical predictions for wave propagation speed, as documented in Section 6.

The particle equation of motion has been integrated by a leapfrog scheme using the classical Boris pusher, properly modified to take into account the ponderomotive envelope component in the Lorentz force. Quadratic grid convergence of numerical error in the particle motion, supporting error analysis of the proposed scheme, has been clearly documented in Section 6.

Besides the ENV/PIC implementation, based on PIC particles, a second integration scheme, denoted as ENV/Fluid, where plasma equation of motion is formulated using Eulerian fluid momentum-density variables, has been presented and tested.

The proposed implementations, ENV/PIC and ENV/Fluid, have been designed on a unitary, self-consistent computational framework. The resulting set of all numerical procedures has been encoded in `ALaDyn-v2018.3` package [25]. The code runs in parallel platforms using standard domain decomposition and MPI procedures. As a preliminary estimate to evaluate the cpu computational resources needed for numerical simulations of realistic LWFA regimes, we take under consideration the ENV/PIC run with $\lambda_0/\Delta z = 10$ and the ENV/Fluid one with $\lambda_0/\Delta z = 18.75$ presented in Fig. 8. We quote a value of $\tau_e \sim 20$ h/mm (run with $N_{p.p.c} = 20$ particles per cell) for ENV/PIC code and $\tau_f \sim 2.5$ h/mm for ENV/Fluid, where both cases were run on 1156 cores on MARCONI (CINECA). Clearly, the comparison has to be made between two converged (in terms of resolution) configurations to correctly estimate the computational time. Anyway, from our measurement, the ENV/Fluid scheme run at $\lambda_0/\Delta z = 10$ takes $\tau_f \sim \tau_e/20$, which confirms that a fluid code is faster by a factor $N_{p.p.c}$ with respect to an ENV/PIC scheme.

Acknowledgments

We would like to thank Carlo Benedetti, for the useful discussions and the precious advices he gave us during the proceeding of this work. We also acknowledge the A. Marocchino grant IsB15_SIPWFA and the P. Londrillo grant IsC65_ENV-LWFA under the ISCRA initiative at CINECA, for the availability of high performance computing resources and support. Also, we acknowledge support from the European Union's Horizon2020 research and innovation programme under grant agreement No.653782 (EuPRAXIA project), and from the MIUR funded Italian research Network ELI-Italy (D.M.n. 631/16).

Appendix A. Reducing dispersive error in the envelope propagation

To envisage optimal (δ_1, δ_2) parameter values in the modified numerical derivatives equation (25), one first considers the numerical dispersion relation of the linear ($\chi = 1$) equation (9), expressed by the eigenvalues of the numerical operators on a Fourier basis $\sim \exp\left[i(\mathbf{k}\cdot\mathbf{x}_g - \omega\Delta t)\right]$:

$$\hat{\Omega}^2 - c^2[\hat{K}_z^2(1+\delta_2(\Delta z)^2\hat{K}_z^2) + \sum_{c=x,y}\hat{K}_c^2] + 2\omega_0[\hat{\Omega} - c\hat{K}_z(1+\delta_1(\Delta z)^2\hat{K}_z^2)] = \omega_p^2 \tag{A.1}$$

where

$$\hat{\Omega}^2 \equiv \frac{\sin^2(\omega\Delta t/2)}{(\Delta t/2)^2}, \quad \hat{\Omega} \equiv \frac{\sin(\omega\Delta t)}{\Delta t}$$
$$\hat{K}_c^2 \equiv \frac{\sin^2(k_c\Delta c/2)}{(\Delta c/2)^2}, \quad \hat{K}_z \equiv \frac{\sin(k_z\Delta z)}{\Delta z}. \tag{A.2}$$

Expanding $\sin(u) = u - u^3/6 + \mathcal{O}(u^5)$, one recovers the exact dispersion relation equation (17) to the leading second order approximation:

$$\omega^2 + 2\omega_0(\omega - ck_z) - c^2(k_z^2 + k_\perp^2 + k_p^2) = TE_1 + TE_2, \tag{A.3}$$

where the truncation errors TE_1 and TE_2, defined as

$$TE_1 = -\frac{\omega_0}{6}[\omega(\omega\Delta t)^2 - ck_z(k_z\Delta z)^2(1+6\delta_1)],$$
$$TE_2 = -\frac{1}{12}[\omega^2(\omega\Delta t)^2 - c^2k_z^2(k_z\Delta z)^2(1+12\delta_2) - c^2\sum_{c=x,y}k_c^2(k_c\Delta c)^2], \tag{A.4}$$

come from the discretized first and second derivatives in time and space, respectively. By expressing the time step size by $\Delta t = \sigma\bar{h}\Delta z$, where σ is the Courant number, and by taking into account that $\omega = ck_z + \mathcal{O}(k_0\varepsilon^2)$, the dispersive numerical errors for wave propagation along the z coordinate can be reduced to the $\mathcal{O}(\varepsilon^2)$ size by selecting $\delta_1 = (\nu^2-1)/6 < 0$, and $\delta_2 = (\nu^2-1)/12 < 0$, where $\nu = \sigma\bar{h}$.

The numerical dispersion relation for the Maxwell equation (31) has the same form of Eq. (A.1) with $\omega_0 = 0$:

$$\hat{\Omega}^2 - c^2\left[\hat{K}_z^2(1+\delta_3(\Delta z)^2\hat{K}_z^2) + \sum_{c=x,y}\hat{K}_c^2\right] = \omega_p^2. \tag{A.5}$$

Now, if $\mathcal{D}_z^{(o)}$ applies only to $\mathcal{D}\times\mathbf{E}$ terms, $\delta_3 = \delta_2$ whereas if it applies also to $\mathcal{D}\times\mathbf{B}$ terms, $2\delta_3 = \delta_2$, as reported in the main text.

Appendix B. Linear stability analysis for the envelope equation

To evaluate the condition for linear stability, the numerical dispersion relation of the discretized envelope equation (26) multiplied by $\Delta t^2/4$ is now expressed by

$$\sin^2\left(\frac{\omega\Delta t}{2}\right) = c^2\Delta t^2\left[\hat{P}_2 + \frac{k_p^2}{4}\right] + \frac{\eta}{2}\hat{P}_1,$$
$$\hat{P}_2 \equiv \sum_c \frac{\sin^2(k_c\Delta c/2)}{\Delta_c^2} + \delta_2\frac{\sin^4(k_z\Delta z)}{\Delta z^2}, \tag{B.1}$$
$$\hat{P}_1 \equiv \frac{c\Delta t}{\Delta z}\sin(k_z\Delta z)[1+\delta_1\sin^2(k_z\Delta z)] - \sin(\omega\Delta t),$$

where $\eta = ck_0\Delta t = \omega_0\Delta t$.

Now, by evaluating each spatial wavenumber k_c, $c = x, y, z$ at the Nyquist frequency $[k_c]_{max} = \pi/\Delta c$, one has the upper bound estimate,

$$\sum_c \frac{\sin^2(k_c\Delta c/2)}{\Delta_c^2} + \delta_1\frac{\sin^4(k_z\Delta z)}{\Delta z^2} < \frac{1}{\bar{h}^2\Delta z^2} + \frac{\delta_1}{\Delta z^2}, \tag{B.2}$$

and then, by inserting the relation defining the Courant number relation $c\Delta t = \sigma\bar{h}\Delta z$,

$$(c\Delta t)^2[\hat{P}_2 + k_p^2/4] < \sigma^2[1 + \bar{h}^2(\Delta z k_p/2)^2 + \delta_2\bar{h}^2]. \tag{B.3}$$

The second term on the right hand side of Eq. (B.1) can be bounded by

$$\hat{P}_1 < \frac{c\Delta t}{\Delta z}[1+4\delta_1], \tag{B.4}$$

and the linear stability condition $\sin^2(\omega\Delta t) < 1$ entails the estimate for the Courant number

$$\sigma \leq \left[1+\bar{h}^2\left(\frac{\Delta z k_p}{2}\right)^2+\delta_2\bar{h}^2+k_0\Delta z\bar{h}^2\frac{1+4\delta_1}{2}\right]^{-1/2} \tag{B.5}$$

We notice, that the same procedure applied to the linearized Maxwell equation for wake fields, gives the standard condition for stability

$$\sigma_0 \leq \left[1+\bar{h}^2\left(\frac{\Delta z k_p}{2}\right)^2+\frac{\delta_2\bar{h}^2}{2}\right]^{-1/2} \tag{B.6}$$

showing that the explicit integration of the envelope wave equation requires only a small correction

$$\sigma \leq \sigma_0\left[1-k_0\Delta z\bar{h}^2\frac{1+4\delta_1}{4}\right], \tag{B.7}$$

depending on the grid resolution $k_0\Delta z$ of laser wavenumber. In Eq. (B.7), the longitudinal cell size Δz is necessarily the same as the one in Eq. (B.6), for consistency reasons.

References

[1] P. Mora, T.M. Antonsen Jr, Phys. Plasmas 4 (1) (1997) 217–229.
[2] B. Quesnel, P. Mora, Phys. Rev. E 58 (3) (1998) 3719.
[3] B. Cowan, D. Bruhwiler, E. Cormier-Michel, E. Esarey, C. Geddes, P. Messmer, K. Paul, J. Comput. Phys. 230 (1) (2011) 61–86.
[4] E.A. Startsev, Phys. Rev. E 55 (6) (1997) 7527.
[5] P. Messmer, D.L. Bruhwiler, Phys. Rev. ST Accel. Beams 9 (2006) 031302, http://dx.doi.org/10.1103/PhysRevSTAB.9.031302.
[6] C. Benedetti, C. Schroeder, E. Esarey, C. Geddes, W. Leemans, AIP Conference Proceedings, vol. 1299, (1) AIP, 2010, pp. 250–255.
[7] C. Benedetti, F. Rossi, C. Schroeder, E. Esarey, W. Leemans, Phys. Rev. E 92 (2) (2015) 023109.
[8] A. Helm, J. Vieria, L. Silva, R. Fonseca, APS Div. Plasma Phys. Meet. (2016) abstract id. GP10011.
[9] C. Benedetti, C. Schroeder, C. Geddes, E. Esarey, W. Leemans, Plasma Phys. Control. Fusion 60 (1) (2017) 014002.
[10] M. Kärkkäinen, E. Gjonaj, T. Lau, T. Weiland, Low-dispersion wake field calculation tools, in: Proc. International Computational Accelerator Physics Conference, 2006.
[11] P. Londrillo, C. Benedetti, A. Sgattoni, G. Turchetti, Nuclear Instrum. Methods Phys. Res. A 620 (2010) 28–35.
[12] A. Pukhov, Proceedings of CAS-CERN Accelerator School: Plasma Wake Acceleration, 23-29 November 2014, Holzer, CERN-2016-001, (CERN, Geneva Switzerland), 2016, pp. 181–206.
[13] R. Lehe, A. Lifschitz, C. Thaury, V. Malka, X. Davoine, Phys. Rev. ST Accel. Beams 16 (2013) 021301.
[14] J.P. Boris, Proceedings of Forth Conference on Numerical Simulation Plasmas, Naval Research Laboratory, Washington, D.C. 1970, 1970, pp. 3–67.
[15] J.L. Vay, Phys. Plasmas 15 (5) (2008) 056701.
[16] D. Gordon, W. Mori, T. Antonsen, A Ponderomotive Guiding Center PIC Code for Modeling Laser-Plasma Accelerations, in: APS Division of Plasma Physics Meeting Abstracts, 1999.
[17] T.Z. Esirkepov, Comput. Phys. Comm. 135 (2) (2001) 144–153.
[18] R.J. LeVeque, Numerical Methods for Conservation Laws, Springer, 1990, pp. 122–135.
[19] S.O. Xu-Dong Liu, T. Chang, J. Comput. Phys. 115 (1) (1994) 200–212.
[20] A. Rehman, S. Qamar, Comput. Math. Appl. 76 (11–12) (2018) 2648–2664.
[21] C.-C. Wu, Geophys. Astrophys. Fluid Dyn. 101 (1) (2007) 37–61.
[22] C. Schroeder, C. Benedetti, E. Esarey, J. van Tilborg, W. Leemans, Phys. Plasmas 18 (8) (2011) 083103.
[23] F. Massimo, S. Atzeni, A. Marocchino, J. Comput. Phys. 327 (2016) 841–850.
[24] A. Marocchino, F. Massimo, A. Rossi, E. Chiadroni, M. Ferrario, Nucl. Instrum. Methods Phys. Res. A 829 (2016) 386–391.
[25] S. Sinigardi, D. Terzani, P. Londrillo, A. Marocchino, F. Massimo, F. Mira, A. Sgattoni, Aladyn/aladyn: Aladyn v2018.3, 2018, http://dx.doi.org/10.5281/zenodo.1477315.